Chemical and Morphological Inhomogeneity of Aluminum Metal and Oxides from Soft X-ray Spectromicroscopy

Alison B. Altman,[1,2] C. Das Pemmaraju,[3] Selim Alayoglu,[1] John Arnold,[1,2] Corwin H. Booth,[1] Augustin Braun,[1] Christopher E. Bunker,[4] Alexandre Herve,[1] Stefan G. Minasian,[1*] David Prendergast,[3*] David K. Shuh,[1] Tolek Tyliszczak[5]

[1] Chemical Sciences Division, Lawrence Berkeley National Laboratory, Berkeley, CA 94720, United States
[2] Department of Chemistry, University of California, Berkeley CA 94720, United States
[3] Molecular Foundry, Lawrence Berkeley National Laboratory, Berkeley, CA 94720, United States
[4] Air Force Research Laboratory, Propulsion Directorate, Wright-Patterson Air Force Base, OH, 45433, United States
[5] Advanced Light Source, Lawrence Berkeley National Laboratory, Berkeley, CA 94720, United States

Email: sgminasian@lbl.gov, dgprendergast@lbl.gov

ABSTRACT. Oxygen and aluminum K-edge X-ray absorption spectroscopy (XAS), imaging from a scanning transmission X-ray microscope (STXM), and first principles calculations were used to probe the composition and morphology of bulk aluminum metal, α- and γ-Al_2O_3, and several types of aluminum nanoparticles. The imaging results agreed with earlier transmission electron microscopy studies that showed a 2 to 5 nm thick layer of Al_2O_3 on all the Al surfaces. Spectral interpretations were guided by examination of the calculated transition energies, which agreed well with the spectroscopic measurements. Features observed in the experimental O and Al K-edge XAS were used to determine the chemical structure and phase of the Al_2O_3 on the aluminum surfaces. For unprotected 18 and 100 nm Al nanoparticles, this analysis revealed an oxide layer that was similar to γ-Al_2O_3 and comprised of both tetrahedral and octahedral Al coordination sites. For oleic-acid protected Al nanoparticles, only tetrahedral Al oxide coordination sites were observed. The results were correlated to trends in the reactivity of the different materials, which suggests that the structures of different Al_2O_3 layers have an important role in the accessibility of the underlying Al metal towards further oxidation. Combined, the Al K-edge XAS and STXM results provided detailed chemical information that was not obtained from powder X-ray diffraction or imaging from a transmission electron microscope.

INTRODUCTION

Efforts to utilize aluminum and other oxophilic metals require a precise grasp of surface structure and composition, as well as passivation techniques to control surface reactivity. Aluminum materials do not exhibit ideal, bulk-like surface terminations, which becomes an increasingly dominant characteristic of their chemistry as the surface-area to volume ratio increases. In the case of aluminum, the metal typically has a ~5 nm passivating layer of Al_2O_3,[1] such that the weight % of O in nanoparticles increases as particle size decreases. Al_2O_3 is commonly found in a number of different amorphous (*am*) and crystalline phases (α and γ, among others). However, relatively little is known about how the coexistence of multiple crystalline structures at an interface can result in heterogeneous oxide systems with unusual porosity, electronic structure, thermodynamic stability, and reactivity. Hence, unraveling the rates and mechanisms of Al metal reactivity with O_2 in fine powders, nanoparticles, thin films, and molecular clusters has been the subject of considerable experimental[2-7] and theoretical effort.[8-13] Understanding how changes in the phase of Al_2O_3 can impact reactivity has important consequences for scientific and technological applications for aluminum in ceramics, catalysis, coatings, separations,[14-20] and energetic materials.[21-25] To optimize the synthesis of well-defined nanoparticles and control their reactivities, characterization tools are needed that can probe the structure of heterogenous materials over multiple length scales and under real-world conditions.

X-ray absorption spectroscopy and scanning transmission X-ray microscopy (STXM-XAS) have emerged as powerful probes of nano- and microscale physical structure and chemical bonding for aluminum materials.[26,27] Each also has unique advantages and limitations when compared with the electron-based analogs scanning transmission electron microscopy (STEM) and electron energy-loss spectroscopy (STEM-EELS).[28] For example, modern STEM capabilities regularly achieve 0.1 nm spatial resolution and monochromated EELS can provide as fine as 0.2 eV energy resolution. STXM can accommodate thicker samples (1 to 20 μm depending on the X-ray probe energy, relative to 0.5 μm for STEM when conducted with a fixed energy electron beam), but the spatial resolution is limited to about 25 nm by the focusing ability of the X-ray optic. Modern STXM instruments easily achieve 0.1 eV energy resolution under normal conditions (resolving power $E/\Delta E > 7500$), and XAS collected in the transmission mode can be obtained from the core-levels of many elements in the Periodic Table, including the light atom K-edges for B, C, N, O, F, Na, Mg, Al, and Si. Previous studies have shown that the spectroscopic accuracy of STXM-XAS[29-32] provides bulk-like electronic structure information that can be interpreted quantitatively within a band structure or molecular orbital model.[33-37] Additionally, X-ray based microscopes are ideally-suited for sensitive inorganic materials because compositional changes or other damaging effects that can occur on exposure to vacuum or to an electron beam are more easily controlled.[38,39]

In this study, images from STXM were used to evaluate the chemical speciation and morphology for several reference materials as well as aluminum nanoparticles prepared under different synthetic conditions. The reference materials included a 100 nm aluminum metal foil, α-Al_2O_3, and γ-Al_2O_3. Aluminum nanoparticles (Al NPs) prepared with three different synthetic methodologies were also explored: core-shell Al NPs with 54 nm average diameters, prepared with a protective organic coating of oleic acid (Al–OA NPs);[40] bare Al NPs with 100 nm average diameters and no protective coating, prepared by the electrical explosion of wires (similar to ALEX®);[39,41] bare Al NPs with 18 nm average diameters

and no protective coating, prepared by pulsed laser ablation of Al targets in an organic solvent.[42,43] These analytes were specifically chosen because they provided a range of particle sizes, compositions, surface chemistries, and reactivities.[44-47] For example, previous studies have shown that protecting agents including organic ligands[40,48-54] and polymer[55-57] or metal coatings[44,58,59] enhanced reactivity properties and provided chemical control over structural attributes like particle size and monodispersity. The STXM-XAS results were consistent with earlier spectromicroscopy studies,[26,55,60] and also revealed new differences in the surface and micron-scale speciation of Al nanoparticles.

RESULTS AND DISCUSSION

Scanning Transmission X-ray Microscopy. The 100 nm Al foil and 18 and 100 nm Al NPs were obtained from commercial sources and used as received (see Experimental). The protected, core-shell Al–OA NPs were prepared according to the literature procedure, and a 54 nm average size was determined by transmission electron microscopy (TEM) (Supporting Information).[40] Powder X-ray diffraction (PXRD) patterns were obtained from all the samples to evaluate the purity of analytes used in subsequent STXM measurements (Supporting Information). In each case, the PXRD patterns were consistent with the presence of predominantly face-centered cubic aluminum metal. For the 100 nm Al NPs, the PXRD measurements also provided evidence for a minor component of hydrated alumina, α-$Al_2O_3 \bullet (H_2O)_3$. No evidence for α-Al_2O_3 was observed in the PXRD patterns from the 18 nm Al NPs and 54 nm Al–OA NPs. However, weak reflections were observed that could not be definitively assigned, and may have been evidence of small amounts of Al_2O_3 present in other polymorphs (e.g., β-, θ-, κ-Al_2O_3).

The STXM at the Molecular Environmental Science beamline 11.0.2 of the ALS was used to collect images, elemental maps, and O and Al K-edge XAS spectra from a 100 nm Al foil and the three different types of Al NPs described above.[61-63] To minimize degradation of the air- and water-sensitive materials, samples were encapsulated between Si_3N_4 supports in an argon-filled glovebox. In addition, the STXM was filled with a partial atmosphere of helium during acquisition. The STXM was used to collect single-energy images and elemental contrast maps by raster-scanning the sample and collecting transmitted monochromatic light as a function of sample position. Figure 1 shows representative normal contrast images and elemental maps from micron-scale aggregates of nanometer-sized particles. Lighter regions in the elemental maps corresponded to greater concentration of the absorbing atom, and were obtained by subtraction of two images: one taken at an energy just below the edge and another taken at the absorption maximum (see "X-ray Absorption Spectroscopy" below). For example, elemental mapping at the Al K-edge was used to identify particles containing metallic aluminum by subtracting an image obtained at 1550 eV from another at 1560 eV. Regions containing Al_2O_3 were identified at the Al K-edge with energies of 1555 and 1571 eV and at the O K-edge with energies of 530 and 540 eV.

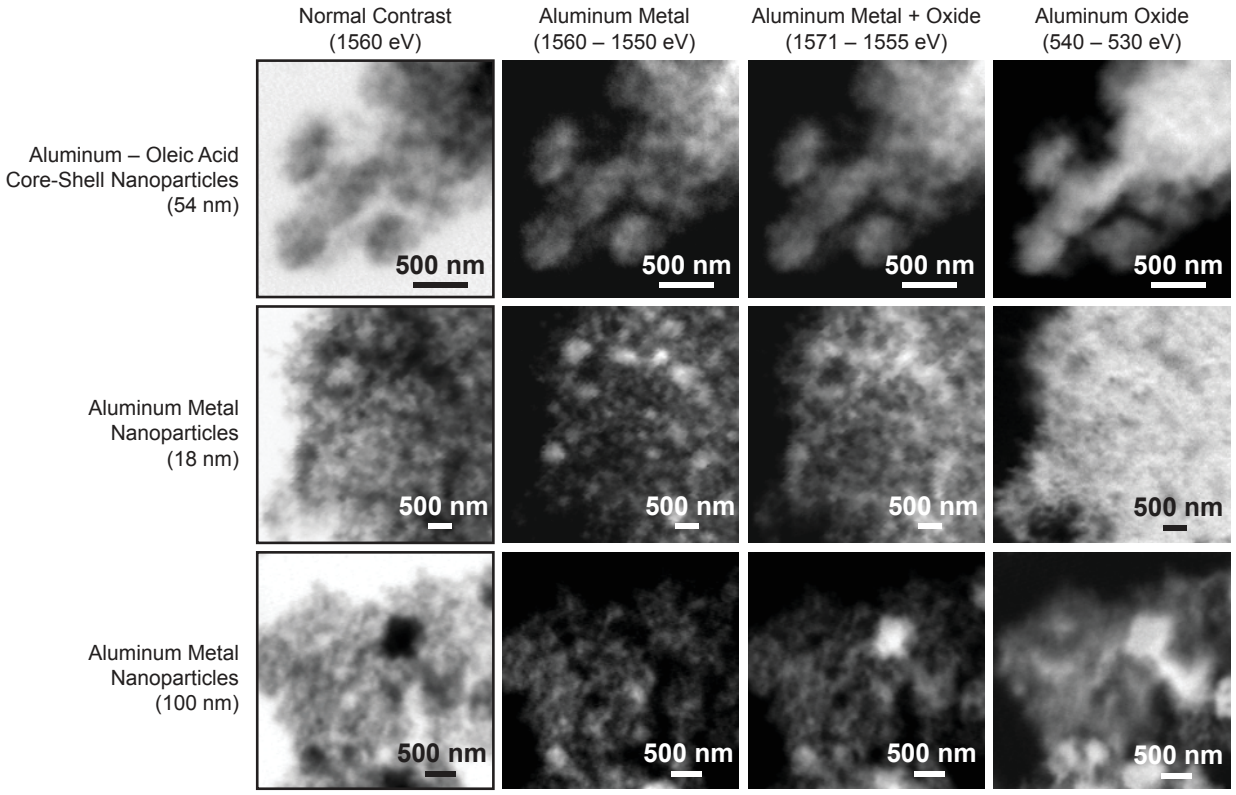

Figure 1. Representative contrast images and elemental difference maps obtained from aggregates of aluminum nanoparticles from which XAS were obtained. Difference maps were produced by obtaining images at the two energies indicated at the top of each column. Subtraction of a background image taken at an energy just below the absorption edge from another image taken at an energy on the absorption maximum generated the difference map, where lighter regions indicate greater concentration of the absorbing atom.

The images in Figure 1 show that all of the NPs had small diameters on the nanometer scale. In powdered form, all the materials formed tight micron-scale aggregates, as had been observed previously for both bare NPs and NPs protected by inorganic and organic surface layers.[55,60,64] Although many details of the nanoscale structure exceeded the spatial-resolution capability of STXM (40 nm under the experimental conditions used), on a large scale the Al–OA NPs were monodispersed and had a uniform distribution of metallic Al and Al_2O_3. In contrast, the STXM images of the 18 and 100 nm Al NPs revealed inhomogeneities in the distribution of metallic aluminum and Al_2O_3, and showed that particle sizes ranged from the nano to the micrometer scale. These observations agreed well with earlier scanning electron microscopy (SEM) and TEM measurements on ALEX® (an ultra-fine aluminum powder produced by the electrical explosion of wires), which showed that while most particle diameters were on the order of 100 nm, particles as small as 20 nm and up to 500 nm in diameter were also observed.[39]

The STXM images shown in Figure 1 did not provide a direct measure of the thickness of the passivating shells of aluminum oxides. However, relative amounts of metallic aluminum and aluminum oxide in the nanomaterials were evaluated from the images by considering the O and Al K-edge spectroscopic results (*vide infra*) and conducting Singular Value Decomposition (SVD) analysis.[65] The optical density of a target area in a given image was governed by $OD = \mu \times \rho \times t$, where μ was the mass absorption coefficient, ρ was the density, and t was the sample thickness or path length. In this study, the intensity of the Al K-edge spectrum (OD) at 1560 eV was proportional to the concentration ($\rho \times t$) of metallic

Al in the target area of a given particle. Similarly, the intensity of the O K-edge spectrum (OD) at 540 eV was proportional to the surface concentration of Al_2O_3 in the same target area. Using these concentrations, values for the weight percent of Al and Al_2O_3 were determined and are given in Table 1. To provide an accurate measurement, analyses encompassed a number of individual particles and were conducted on large target areas greater than 10 μm^2 and 10,000 total pixels. The chemical composition of surface species was identified from the O and Al K-edge XAS results (*vide infra*). It is worth noting that a limitation of the SVD approach arose from the assumption that surfaces are comprised of a single phase of Al_2O_3, when a more complex mixture of multiple oxide phases, hydroxides, and hydrated surface species may have been present.

Table 1. Characteristics of Al metal and nanoparticle materials determined from STXM–XAS. For nanoparticle-based samples, estimation of the oxide layer thickness (t_{oxide}) was based on the relative weight percents of each constituent, and assumed an idealized spherical morphology with a homogenous layer of γ-Al_2O_3 (ρ = 3.7 g cm^{-3}). For the 100 nm Al foil, estimation of t_{oxide} was based on a homogenous layer of *am*-Al_2O_3 (ρ = 2.3 g cm^{-3}).[a] Complete details on the derivation of t_{oxide} are provided in the Supporting Information.

				Weight % of Constituents			
Cmpd	diameter (nm)	passivation	Source	OA	Al_2O_3	metallic Al	t_{oxide} (nm)
Al foil	100	air	Luxel	–	12 ± 1	88 ± 8	3.9 ± 0.4
Al NPs	18	air	US Nano	–	53 ± 5	47 ± 4	1.7 ± 0.2
Al NPs	100	air	US Nano	–	34 ± 3	66 ± 6	5.2 ± 0.5
Al–OA NPs	54	oleic acid	this work	13 ± 1	29 ± 2	58 ± 5	2.3 ± 0.4

[a] Values for the density of *am*-Al_2O_3 vary widely.[66] Using ρ = 3.6 g cm^{-3} for *am*-Al_2O_3 provides r_{oxide} = 2.5 ± 0.3 nm for the 100 nm Al foil.

For the Al foil described above, this analysis showed that the foil had surface concentrations of 3.6 ± 0.3 μg cm^{-2} oxygen and 56 ± 4.0 μg cm^{-2} aluminum. If all the oxygen was associated with a layer of amorphous alumina (*am*-Al_2O_3, ρ = 2.3 g/cm^3),[38] then these values correspond to 88 ± 8 wt. % metallic aluminum and 12 ± 1 wt. % *am*-Al_2O_3. The thickness of the foil (104 ± 11 nm) was calculated by dividing the surface concentration by density of aluminum metal. Likewise, the thicknesses of Al_2O_3 layers on the top and bottom of the Al foil were calculated at 3.9 ± 0.4 nm each depending on the value for the density of *am*-Al_2O_3 used. These values are similar to specifications for the Al foil quoted by the manufacturer,[67] which include thicknesses of 100 and 5 nm and compositions of roughly 86 and 14 wt. % for Al metal and *am*-Al_2O_3, respectively.

Relative amounts of Al metal and oxide for the conventionally-synthesized nanoparticles were determined using SVD analysis in a similar fashion (Table 1). The 18 nm Al NPs had 53 ± 5 wt. % Al_2O_3 and 47 ± 4 wt. % metallic Al, and the 100 nm Al NPs had 34 ± 3 wt. % Al_2O_3 and 66 ± 6 wt. % metallic Al. As described in the introduction, these changes in composition were anticipated given the increased fraction of metallic Al in larger particles. The STXM derived values suggested that there is somewhat less metallic Al in the 100 nm nanoparticles used in this study (66 ± 6 wt. %) than was determined for a different sample of 100 nm ALEX® NPs using a volumetric analysis (86% metallic Al) and using energy dispersive spectroscopy (EDS) from TEM (90 ± 5 wt. % total Al and 10 ± 2 wt. % O, which corresponded to 79 ± 5 wt. %

metallic Al and 21 ± 4 wt. % Al_2O_3).[41,68] As described above for the Al foil, these relative amounts of Al and Al_2O_3 were also used to calculate thicknesses for the Al_2O_3 passivation layer by assuming an ideal spherical morphology and monodisperse 18 and 100 nm particle diameters (Table 1 and Supporting Information). This analysis showed that the conventionally-synthesized 18 nm and 100 nm Al NPs had 1.7 ± 0.2 and 5.2 ± 0.5 nm thick Al_2O_3 layers, respectively.

For the Al–OA core-shell nanoparticles, proportions of 58 ± 5, 29 ± 2, 13 ± 1 wt. % were calculated for the metallic core, Al_2O_3, and carbonaceous organic layer, respectively. For comparison, previous ICP-MS and TGA studies have suggested that 40% of the sample mass was metallic aluminum, 25% was Al_2O_3, and 35% was organic.[40] In both cases, the amount of oxygen relative to carbon was larger than anticipated for oleic acid alone, and clearly indicates that oleic acid passivation did not completely inhibit growth of an aluminum oxide layer. This observation is consistent with earlier studies, which showed that passivation resulted in decomposition of the oleic acid and formation of an organic outer layer on the surface on an intermediate oxide layer.[40] A thickness of 2.3 ± 0.4 nm was estimated for the Al_2O_3 passivation layer in the Al–OA NPs, which is also in agreement with earlier work showing that organic or inorganic protective coatings limited growth of the Al_2O_3 layer to about 2 nm.[44,55,69]

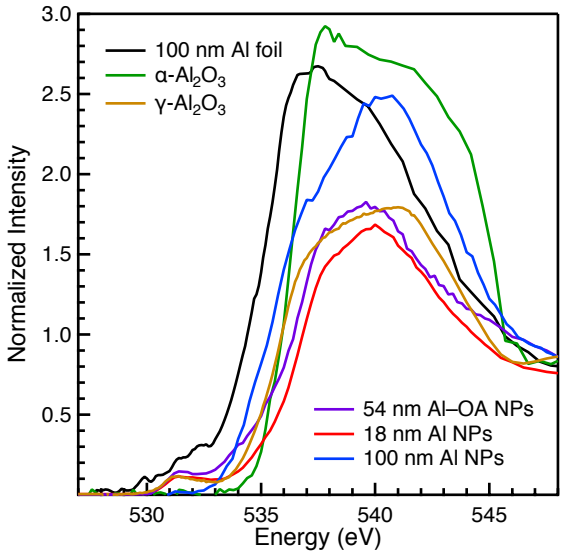

Figure 2. O K-edge XAS data for 54 nm Al–OA nanoparticles (purple), 18 nm Al NPs (red), 100 nm Al NPs (blue), and reference materials including a 100 nm Al metal foil (black), α-Al_2O_3 (green) and γ-Al_2O_3 (brown).

X-ray Absorption Spectroscopy. Figure 2 shows the background-subtracted and normalized oxygen K-edge XAS measured from the bare 18 and 100 nm Al NPs, core-shell Al–OA NPs, and reference materials α-Al_2O_3, γ-Al_2O_3, and a 100 nm Al foil. As previous studies have shown,[11,30,38] differences in the O K-edge XAS can reflect changes in Al–O bonding found for different phases of aluminum oxides and hydroxides. The O K-edge spectra shown in Figure 2 were similar in many regards; however, some important differences were readily apparent. For example, the spectrum for γ-Al_2O_3 exhibited a small shoulder near 531 – 532 eV that was not observed for α-Al_2O_3. Previous work by Århammar and coworkers suggested that these small features are characteristic of O–O interactions that are present in some phases of

Al_2O_3 but not in crystalline α-Al_2O_3.[38] The spectra from the 18 and 100 nm Al NPs and Al–OA NPs each had some of the spectroscopic signatures observed from γ-Al_2O_3. None of the nanoparticle spectra resembled the O K-edge of the 100 nm Al foil (reflecting *am*-Al_2O_3), which was shifted such that the first inflection point was approximately 1 eV lower in energy than was observed for the other materials.

Al K-edge XAS was used to further elaborate on the compositional assignments determined using O K-edge XAS. Figure 3 shows representative background subtracted and normalized Al K-edge spectra obtained from the bare 18 and 100 nm Al NPs, core-shell Al–OA NPs, and reference materials α-Al_2O_3, γ-Al_2O_3, and the 100 nm Al foil. Energies and assignments for the spectral features are summarized in Table 2. Because previous attempts to model and interpret Al K-edge XAS data for the metal and oxide references have been limited,[31,70,71] this discussion will begin by establishing the bonding descriptions needed to justify the spectral assignments for the nanoparticle materials given in Table 2.

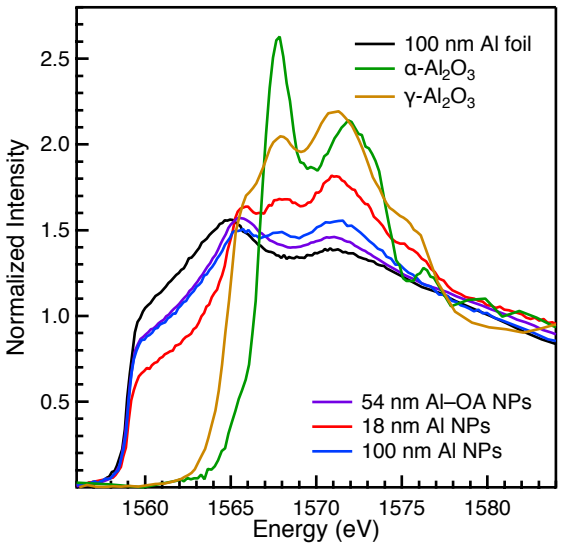

Figure 3. Al K-edge XAS for 54 nm Al–OA nanoparticles (purple), 18 nm Al NPs (red), 100 nm Al NPs (blue), and reference materials including a 100 nm Al metal foil (black), α-Al_2O_3 (green), and γ-Al_2O_3 (brown).

Table 2. Al K-edge feature energies and assignments.

Compound	Energy (eV)	Assignment
α-Al_2O_3	1564.9[a]	1s → 2s-σ* (a_{1g})
	1567.8	1s → 3p-σ/π* (t_{1u})
	1571.9	1s → 3d-σ* (t_{2g})
γ-Al_2O_3	1565.4	1s → 3p-σ/π* (t_2)
	1568.0	1s → 3p-σ/π* (t_{1u})
	1571.2	1s → 3d-σ* (t_{2g})
100 nm Al foil	1559.0	1s → 3p-π[b]
	1564.9	1s → 3p-σ*
	1570.8	1s → 3d-σ*
18 nm Al NPs	1559.0	1s → 3p-π[b]
	1565.9	1s → 3p-σ/π* (t_2)
	1568.0	1s → 3p-σ/π** (t_{1u})
	1571.1	1s → 3d-σ* (t_{2g})
100 nm Al NPs	1559.0	1s → 3p-π[b]
	1565.6	1s → 3p-σ/π* (t_2)
	1567.8	1s → 3p-σ/π* (t_{1u})
	1571.1	1s → 3d-σ* (t_{2g})
54 nm Al–OA NPs	1559.0	1s → 3p-π[b]
	1565.6	1s → 3p-σ/π* (t_2)
	1570.9	1s → 3d-σ*

[a] This transition is weak and dipole-forbidden, but becomes recognizable as a result of some distortion from idealized O_h symmetry which may facilitate some Al 3s and 3p mixing.

Bulk Aluminum Metal. Figure 4 shows the experimental Al K-edge XAS of a 100 nm Al foil and simulations provided by both FEFF 10.0.1[72,73] and XCH DFT calculations. Both theoretical approaches provided good agreement with the experimental data in both the near-edge and extended energy regions. The onset of the Al K-edge for Al metal, defined by the first inflection point, was fixed at 1559.0 eV and was the calibration point for the other Al K-edge spectra described

below. At higher energies, the edge region was characterized by two very broad features at 1564.9 and 1570.8 eV. Although Al K-edge spectra of Al metal have been reported,[74-81] to the best of our knowledge no detailed interpretation of the spectral profile has been provided. The discussion below begins by constructing the band structure model for Al metal that was used to understand the Al K-edge XAS features.

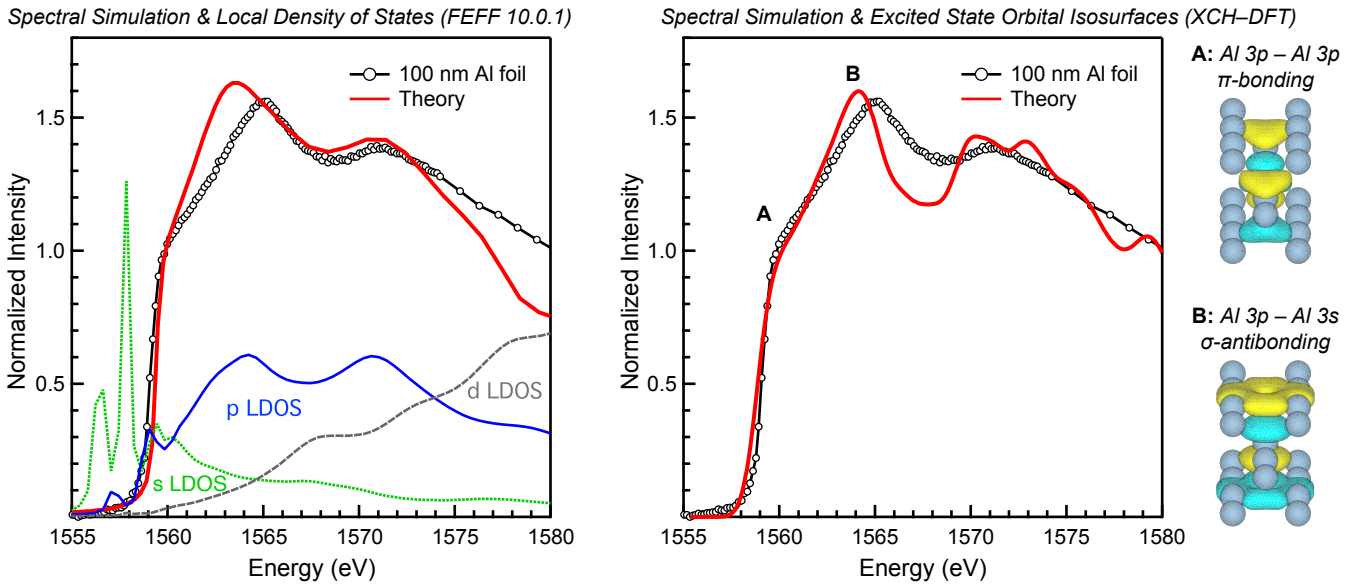

Figure 4. Al K-edge XAS of Al metal (black circles) compared with simulations from FEFF (left) and XCH-DFT (right) calculations. In the left plot, the total simulation (red) is included with the local density of states (LDOS) derived from the FEFF for final states associated with the Al s, p, or d orbitals (green, blue, and gray). In the right plot, the correspondence between transitions and isosurfaces is indicated by the letters A and B. Note that the FEFF calculation is shifted down by approximately 5 eV to better compare to the Al K edge experimental data, which is a typical absolute energy disagreement for FEFF. Similarly, the XCH-DFT simulation was shifted by +1560.65 eV.

From a chemistry perspective, molecular orbital theory can provide a useful starting point for understanding metallic bonding.[82-84] Figure 5 illustrates this approach for the construction of molecular orbitals in aluminum metal, beginning with the hypothetical aluminum molecule Al_2. To a first approximation, interaction of the two 3s atomic orbitals results in formation of two molecular orbitals of σ-symmetry, which are split in energy as the bonding and antibonding combinations. Similarly, the six 3p orbitals form bonding and antibonding orbitals with both σ- and π-symmetries. Furthermore, because the 3s and 3p σ-bonding orbitals have the same symmetry and similar energies (11.3 and 5.9 eV, respectively),[84] they can interact via s-p mixing to form new orbitals with different energies. Castleman et al. have previously used vacuum ultraviolet photoelectron imaging to highlight the importance of s-p hybridization in small aluminum clusters formed in the gas phase.[85] Consequently, Al_2 has a ground-state electronic configuration of $(1\sigma_g^+)^2(1\sigma_u^+)^2(1\pi_u)^2$ where the partially occupied $1\pi_u$ orbitals are bonding, and the empty $2\sigma_g^+$ orbitals are best described as non-bonding resulting from s-p mixing. The orbitals described for Al_2 are split again when an infinite array of Al atoms are brought together in the metal, resulting in a band of tightly packed energy levels corresponding to both bonding and antibonding states.

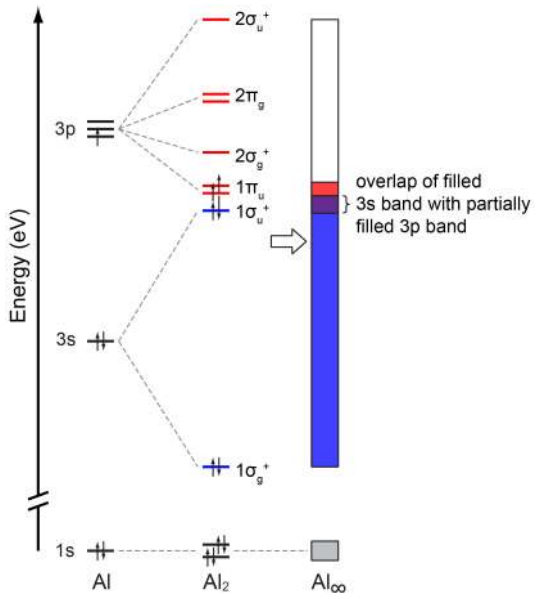

Figure 5. Formation of energy bands in aluminum metal. Orbitals for an isolated Al atom (left) form σ- and π-type interactions in a diatomic molecule (middle) which are split into bonding and antibonding counterparts. Bringing together a large number of atoms in an extended lattice results in a larger number of closely spaced energy levels.

This qualitative picture is consistent with the quantitative Al K-edge XAS simulations obtained using FEFF 10.0.1 and XCH-DFT, shown in Figure 4. As expected, the local density of states provided by the FEFF calculation showed that the occupied bands have predominantly 3s character, while at higher energies the unoccupied bands have primarily Al 3p character. In addition, XCH-DFT calculations were used to generate isosurface plots of the final state electronic orbitals that corresponded to (A) the most dominant transitions near the edge onset, and (B) transitions that were close to the energy of the first main feature at 1564.9 eV (Figure 4). Consistent with the qualitative interpretation provided above, the orbital isosurfaces showed that transitions near the edge onset at 1559 eV involved low–lying empty states with significant π-bonding character between adjacent atoms in the unit cell (Al 1s → π^b). The calculations also showed an additional feature at 1563.6 eV (FEFF) and 1564.2 eV (XCH-DFT), which corresponded to the broad peak at 1564.9 eV in the experimental spectrum. The peak was reminiscent of a shape resonance: broad features associated with short-lived final states, given the increasing probability of decay to the continuum at energies above the Al 1s ionization potential.[86] The orbital isosurfaces in Figure 4 confirmed this interpretation and showed that the states associated with the feature at 1564.9 eV were best described as σ-antibonding between one Al 3p orbital and additional Al 3s orbitals in the plane above and below. Finally, the feature at 1570.8 eV in the experimental and simulated spectra was not easily assigned using the simple band structure provided above; however, the LDOS provided by the FEFF calculations indicated that transitions to states with some Al 3p and Al 3d character may have been present.

Aluminum Oxides. The background-subtracted and normalized Al K-edge XAS of α- and γ-Al_2O_3 are shown in Figure 3. The edge onset for each of the oxides was several eV higher in energy relative to the Al foil. These shifts to higher energy for trivalent oxides resulted from an increase in effective nuclear charge and concomitant stabilization of the Al 1s core levels. Previous Al K-edge analyses of α-Al_2O_3 and other aluminum oxides and minerals have provided frameworks for

assigning transitions in the Al K-edge XAS by constructing models for Al–O bonding in both tetrahedral or octahedral coordination environments.[27,87-91] A similar approach was applied here to develop interpretations of the Al K-edge spectra of α- and γ-Al_2O_3 that could be related to the nanoparticle systems.

The α-Al_2O_3 spectrum had a weak shoulder at 1564.9 eV and two main features at 1567.8 and 1571.9 eV, and closely resembled previously published spectra.[27,87-91] In their detailed examination of aluminosilicate minerals, Li and coworkers developed assignments by comparing Al K-edge and Si K-edge spectra and using MO calculations of the AlO_6^{9-} cluster. Using their assignments for α-Al_2O_3, the very weak and low energy shoulder at 1564.9 eV was assigned to dipole-forbidden transitions from the Al 1s into Al 3s and O 2p antibonding orbitals of a_{1g} symmetry. The first main feature at 1567.8 eV was assigned to transitions from the Al 1s orbitals into Al 3p and O 2p antibonding orbitals of t_{1u} symmetry. The second main feature at 1571.9 eV was assigned to transitions from the Al 1s to final states derived from the Al 3d orbitals of t_{2g} symmetry.

The γ-phase of Al_2O_3 has a spinel-type structure consisting of both octahedral and tetrahedral Al coordination sites; hence, the Al K-edge spectrum of γ-Al_2O_3 was regarded as a superposition of Al K-edge spectra involving the two different symmetries. For example, the two main features at 1568.0 and 1571.2 eV reflected the octahedral coordination environment for Al and were assigned to Al 1s → t_{1u} and Al 1s → t_{2g} transitions as described above for α-Al_2O_3. Using assignments developed previously for γ-Al_2O_3 and aluminosilicate minerals with strictly tetrahedral Al coordination sites,[74,90] the low-energy shoulder at 1565.4 eV in the Al K-edge XAS of γ-Al_2O_3 was assigned to transitions from Al 1s orbitals into Al 3p and O 2p antibonding orbitals of t_2 symmetry. The 2.6 eV increase in energy for Al 1s → t_{1u} transitions relative to the Al 1s → t_2 transitions was attributed to an increase in Al–O overlap expected for six-coordinate octahedral environments.[92] Finally, the additional high-energy shoulder observed at approximately 1575 eV was attributed to a transition from the Al 1s to final states derived from the Al 3d orbitals of e symmetry.

Aluminum Nanoparticles. The spectra from the unsupported metallic Al foil and nanoparticles each exhibited an edge feature at 1559 eV, which indicated that metallic aluminum was a significant component of the nanoparticle materials. However, the Al K-edge spectra also exhibited rich spectral detail reflecting differences in the surface chemistry. For example, each of the nanoparticle materials had a feature between 1565.6 – 1565.9 eV that was not observed in the spectrum from the Al foil. In addition, α-Al_2O_3, γ-Al_2O_3 and both the 18 and 100 nm Al NPs had features at near 1568 eV that were not observed in the spectrum from either the Al foil or the Al–OA NPs. These differences were associated changes in the nature of the oxide layer, and were rationalized by considering the assignments developed above.

The spectral profiles for the conventionally-synthesized 18 and 100 nm Al NPs and the protected Al–OA NPs were similar in that clearly-resolved features with similar intensities and energies were observed at 1565.9, 1565.6, and 1565.6 eV, respectively. These features were also equivalent in energy to those assigned as Al 1s → t_2 transitions observed in the Al K-edge XAS of γ-Al_2O_3 (1565.4 eV). The 18 and 100 nm Al NPs were unique in that they also had features in the Al K-edge XAS at intermediate energies of 1568.0 and 1567.8 eV, and also at higher energies of 1571.1 eV for both, which were recognized as distinct from those observed from the Al foil. These intermediate features were very close to the energy observed for the Al 1s → t_{1u} transitions in the Al K-edge spectrum of both α-Al_2O_3 (1567.8 eV) and γ-Al_2O_3 (1568.0 eV).

Likewise, the higher energy features were similar to the Al 1s → t_{2g} transitions observed for γ-Al_2O_3 (1571.2 eV). Taken together, these observations showed that the oxidation of 18 and 100 nm Al NPs results in formation an oxide layer containing both tetrahedral and octahedral Al coordination sides, which was similar to the γ-phase of Al_2O_3. Oxidation of the Al–OA NPs also resulted in formation of an Al_2O_3 layer containing tetrahedral Al coordination sites; however, no signatures of octahedral Al coordination sites were detected.

Conclusion

The results provided in this study have shown that soft X-ray spectromicroscopy can provide unique insight into the complex interfacial chemistry of electropositive, oxophilic metals such as aluminum. Because exposure to vacuum or an electron beam can induce compositional changes in some nanoscale particles and surfaces, spectromicroscopy measurements were conducted at ambient pressure with soft X-rays to ensure that quantitative information was obtained.[38,39] The normal contrast images and respective elemental maps showed that the thickness of the oxide layer was between 2 and 5 nm for all the aluminum materials studied. The images also showed that the oxide was evenly distributed in oleic-acid protected NPs; however, there was more oxide inhomogeneity in bare, unprotected 18 and 100 nm Al NPs. Features in the Al K-edge XAS of the aluminum nanoparticles were also compared with spectra obtained from reference materials including α-Al_2O_3, γ-Al_2O_3, and a 100 nm aluminum metal film. This comparison revealed that the oleic acid protected nanoparticles had an oxide layer with primarily tetrahedral Al coordination sites, while oxidation of the unprotected 18 and 100 nm Al NPs resulted in formation of both octahedral and tetrahedral coordination sites (similar to those found in γ-Al_2O_3). These observations are consistent with previously published results, and also provided new quantitative insight that was not obtained from analysis of PXRD patterns and TEM images alone. Combined, these results support the viewpoint that advanced synthetic strategies including organic passivation do not eliminate surface oxidation of aluminum metal, but can be used to tune the chemistry of the oxide layer and control its reactivity.[40]

Experimental

General Synthetic Details. All reactions were performed either using standard Schlenk line techniques or in a MBraun inert atmosphere glovebox under a purified nitrogen atmosphere (<0.1 ppm O_2/H_2O). The aluminum foil filter (100 nm thickness) and aluminum nanopowders was purchased from Luxel Corporation and US Research Nanomaterials, Inc, respectively, and used as received. Oleic acid aluminum core-shell nanoparticles were synthesized according to the literature procedure and dried before use.[40] α and γ-Al_2O_3 were purchased from Aldrich and Strem and dried at 100 °C and 1 x 10^{-3} torr for 24 h before use. Sample preparation and methodology for handling air-sensitive analytes was similar to that described previously.[29,31,93] Samples were prepared in an argon-filled glovebox by grinding crystals of the analyte into a fine powder with a mortar and pestle, and brushing the powder onto a Si_3N_4 membrane (100 nm, Silson) with a fiber. This method arranged a large number of micron-scale crystals that were suitable for Al K-edge measurements in a relatively compact area. A second membrane was placed over the sample, and the edges were sealed together using Hardman

Double/Bubble® 5 minute epoxy.

Beamline Characteristics. STXM methodology was similar to that discussed previously.[88-91] Single-energy images and Al K-edge XANES spectra were acquired using the STXM instrument at the Molecular Environmental Science (MES) beamline 11.0.2 at the Advanced Light Source (ALS), which was operated in topoff mode at 500 mA, in a ~0.5 atm He-filled chamber.[61-63] The beamline used photons from an elliptically polarizing undulator that delivers photons in the 100 to 2000 eV energy range to a variable-included-angle plane-grating monochromator. For Al K-edge measurements, the photon energy of the high energy diffraction grating (1100 lines/mm) was calibrated to the Al K-edge from the 100 nm aluminum foil filter sample (inflection point = 1559.0 eV). Both of the 4-jaw exit slit widths were set to 30 μm. The maximum energy resolution $E/\Delta E$ was previously determined at better than 7500, which was consistent with the observed standard deviation for spectral transitions of ± 0.3 eV determined from comparison of spectral features over multiple samples and beam runs. For these measurements, the X-ray beam was focused with a 40 nm zone plate onto the sample, and the transmitted light was detected with a photomultiplier tube. Images at a single energy were obtained by raster-scanning the sample and collecting transmitted monochromatic light as a function of sample position. Spectra at particular regions of interest on the sample image were extracted from the "stack", which is a collection of images recorded at multiple, closely spaced photon energies across the absorption edge. Dwell times used to acquire an image at a single photon energy were 2 ms per pixel. To quantify the absorbance signal, the measured transmitted intensity (I) was converted to optical density using Beer–Lambert's law: $OD = \ln(I/I_0) = \mu\rho d$, where I_0 is the incident photon flux intensity, d is the sample thickness, and μ and ρ are the mass absorption coefficient and density of the sample material, respectively. Incident beam intensity was measured through the sample-free region of the Si_3N_4 windows. Regions of particles with an absorption of >1.5 OD were omitted to ensure the spectra were in the linear regime of the Beer–Lambert law. The data were background subtracted using the *MBACK* algorithm in *MATLAB*,[94] and peak positions were determined from derivative plots generated using the program IGOR 6.0.

FEFF Calculations. FEFF 10.0.1[72,73] calculations utilized a Hedin-Lundqvist potential and converged using a self-consistent field approximation within a 6.0 Å cluster of 79 atoms and a full-multiple scattering expansion using a cluster of 55 atoms within a radius 6.6 Å. All other options were chosen to be default.

Al K-edge Spectral Simulations. XAS at the Al K-edge were calculated using the excited electron and core-hole approach (XCH).[94] The XCH approach has been described previously in detail.[94-96] In this method, the lowest energy X-ray excited state of the system is modeled within an occupation-constrained DFT framework employing a periodic supercell formalism wherein the core-excited atom is described through a core-hole pseudopotential and the screening due to the excited electron is taken into account self-consistently. Higher–lying X-ray excited state energies are approximated through eigenvalue differences obtained from the Kohn-Sham (KS) spectrum of the lowest energy core-excited state. X-ray transition matrix elements are calculated using Fermi's golden rule and typically for light-element K-edges, within a dipole approximation. The XCH method was utilized as implemented in a development version of the Quantum-Espresso package[97] which provides a plane-wave pseudopotential DFT framework for electronic structure calculations. Ultra-soft pseudopotentials[98] with the following valence electronic configurations were employed: $Al(3s^23p^1)$, $O(2s^22p^4)$. These were used together with

a plane-wave energy cut-off of 25 Ry. To describe 1s core-excited Al in XANES simulations, a core-hole pseudopotential with the electronic configuration $1s^1 2s^2 2p^6 3s^2 3p^2$ was generated. A 3 x 3 x 3 supercell consisting of 108 atoms was used. The Brillouin zone was sampled through a 3 x 3 x 3 Γ-centered k-point grid during the Kohn-Sham self-consistent field calculation, but the band structure was interpolated over a uniform Γ-centered 5 × 5 × 5 k-point grid using the Shirley interpolation scheme[99] in order to generate XANES spectra. Within the XCH approach, the relative energy alignment of XAS corresponding to core-excitations on atoms in different chemical environments is carried out through total energy differences.[95] However, since the method is based on core-hole pseudopotentials and does not explicitly include the energy of core electrons, calibration of the absolute energy position of the calculated spectra with respect to experiment involves a rigid energy shift Δ, which was determined to be 1560.65 eV at the Al K-edge based on the inflection point of the onset of absorption. Orbital isosurfaces were visualized using VESTA-3.[100]

Acknowledgments

ABA acknowledges support by a Department of Energy (DOE) Integrated University Program Fellowship at the University of California, Berkeley. This research was supported by the Director, Office of Science, Office of Basic Energy Sciences, Division of Chemical Sciences, Geosciences, and Biosciences Heavy Element Chemistry Program of the U.S. DOE at LBNL under Contract No. DE-AC02-05CH11231. Work at the Molecular Foundry was supported by the Office of Science, Office of Basic Energy Sciences, of the U.S. Department of Energy under Contract No. DE-AC02-05CH11231. Calculations were performed on the Cray XE6 Hopper computer at the National Energy Research Scientific Computing Center (NERSC-LBNL) and Molecular Foundry computing resources, Nano and Vulcan, managed by the High Performance Computing Services Group of LBNL. Research at beamline 11.0.2 at the ALS was supported by the Director, Office of Science, Office of Basic Energy Sciences, Division of Chemical Sciences, Geosciences, and Biosciences Condensed Phase and Interfacial Molecular Sciences Program of the U.S. DOE at LBNL under Contract No. DE-AC02-05CH11231.

Supporting Information Available: Additional details on the compositional analysis, X-ray absorption spectra, and powder X-ray diffraction data. This material is available free of charge via the Internet at http://pubs.acs.org.

References

(1) Fujii, H.; Nakae, H.; Okada, K. Interfacial Reaction Wetting in the Boron-Nitride Molten Aluminum System. *Acta Metall.* **1993**, *41*, 2963-2971.

(2) Trunov, M. A.; Schoenitz, M.; Zhu, X. Y.; Dreizin, E. L. Effect of Polymorphic Phase Transformations in Al_2O_3 Film on Oxidation Kinetics of Aluminum Powders. *Combust. Flame* **2005**, *140*, 310-318.

(3) Luo, Z.; Grover, C. J.; Reber, A. C.; Khanna, S. N.; Castleman, A. W., Jr. Probing the Magic Numbers of Aluminum-Magnesium Cluster Anions and Their Reactivity toward Oxygen. *J. Am. Chem. Soc.* **2013**, *135*, 4307-4313.

(4) Neumaier, M.; Olzmann, M.; Kiran, B.; Bowen, K. H.; Eichhorn, B.; Stokes, S. T.; Buonaugurio, A.; Burgert, R.; Schnoeckel, H. The Reaction Rates of O_2 with Closed-Shell and Open-Shell Al_x^- and Ga_x^- Clusters under Single-Collision Conditions: Experimental and Theoretical Investigations toward a Generally Valid Model for the Hindered Reactions of O_2 with Metal Atom Clusters. *J. Am. Chem. Soc.* **2014**, *136*, 3607-3616.

(5) Smith, J. C.; Reber, A. C.; Khanna, S. N.; Castleman, A. W., Jr. Boron Substitution in Aluminum Cluster Anions: Magic Clusters and Reactivity with Oxygen. *J. Phys. Chem. A* **2014**, *118*, 8485-8492.

(6) Guerieri, P. M.; DeCarlo, S.; Eichhorn, B.; Connell, T.; Yetter, R. A.; Tang, X.; Hicks, Z.; Bowen, K. H.; Zachariah, M. R. Molecular Aluminum Additive for Burn Enhancement of Hydrocarbon Fuels. *J. Phys. Chem. A* **2015**, *119*, 11084-11093.

(7) Luo, Z.; Reber, A. C.; Jia, M.; Blades, W. H.; Khanna, S. N.; Castleman, A. W., Jr. What determines if a ligand activates or passivates a superatom cluster? *Chem. Sci.* **2016**, *7*, 3067-3074.

(8) Ching, W. Y.; Ouyang, L.; Rulis, P.; Yao, H. *Ab Initio* Study of the Physical Properties of γ-Al_2O_3: Lattice Dynamics, Bulk Properties, Electronic Structure, Bonding, Optical Properties, and ELNES/XANES Spectra. *Phys. Rev. B* **2008**, *78*, 014106.

(9) Peintinger, M. F.; Kratz, M. J.; Bredow, T. Quantum-chemical study of stable, meta-stable and high-pressure alumina polymorphs and aluminum hydroxides. *J. Mater. Chem. A* **2014**, *2*, 13143-13158.

(10) Aryal, S.; Rulis, P.; Ouyang, L.; Ching, W. Y. Structure and Properties of the Low-Density Phase ι-Al_2O_3 from First Principles. *Phys. Rev. B* **2011**, *84*, 174123.

(11) Wu, H.; Lu, D.; Zhu, K.; Xu, G.; Wang, H. Crystalline and electronic structure of epitaxial γ-Al_2O_3 films. *Physica B Condens. Matter* **2013**, *413*, 105-108.

(12) Filatova, E. O.; Konashuk, A. S. Interpretation of the Changing the Band Gap of Al_2O_3 Depending on Its Crystalline Form: Connection with Different Local Symmetries. *J. Phys. Chem. C* **2015**, *119*, 20755-20761.

(13) Filatova, E. O.; Konashuk, A. S.; Schaefers, F.; Afanas'ev, V. V. Metallization-Induced Oxygen Deficiency of γ-Al_2O_3 Layers. *J. Phys. Chem. C* **2016**, *120*, 8979-8985.

(14) Zhang, Z. R.; Hicks, R. W.; Pauly, T. R.; Pinnavaia, T. J. Mesostructured forms of γ-Al_2O_3. *J. Am. Chem. Soc.* **2002**, *124*, 1592-1593.

(15) Hicks, R. W.; Pinnavaia, T. J. Nanoparticle assembly of mesoporous AlOOH (boelamite). *Chem. Mater.* **2003**, *15*, 78-82.

(16) Trueba, M.; Trasatti, S. P. γ-Alumina as a support for catalysts: A review of fundamental aspects. *Eur. J. Inorg. Chem.* **2005**, 3393-3403.

(17) Yuan, Z. Y.; Ren, T. Z.; Azioune, A.; Pireaux, J. J.; Su, B. L. Self-assembly of hierarchically mesoporous-macroporous phosphated nanocrystalline aluminum (oxyhydr)oxide materials. *Chem. Mater.* **2006**, *18*, 1753-1767.

(18) Busca, G. Acid Catalysts in Industrial Hydrocarbon Chemistry. *Chem. Rev.* **2007**, *107*, 5366-5410.

(19) Marquez-Alvarez, C.; Zilkova, N.; Perez-Pariente, J.; Cejka, J. Synthesis, characterization and catalytic applications of organized mesoporous aluminas. *Cat. Rev. - Sci. Eng.* **2008**, *50*, 222-286.

(20) Yuan, Q.; Yin, A. X.; Luo, C.; Sun, L. D.; Zhang, Y. W.; Duan, W. T.; Liu, H. C.; Yan, C. H. Facile synthesis for ordered mesoporous γ-aluminas with high thermal stability. *J. Am. Chem. Soc.* **2008**, *130*, 3465-3472.

(21) Wang, Z. W.; Yi, X. Z.; Li, G. Z.; Guan, D. R.; Lou, A. J. A functional theoretical approach to the electrical double layer of a spherical colloid particle. *Chem. Phys.* **2001**, *274*, 57-69.

(22) Kwok, Q. S. M.; Fouchard, R. C.; Turcotte, A. M.; Lightfoot, P. D.; Bowes, R.; Jones, D. E. G. Characterization of aluminum nanopowder compositions. *Propell. Explos. Pyrot.* **2002**, *27*, 229-240.

(23) Kwon, Y. S.; Gromov, A. A.; Ilyin, A. P.; Rim, G. H. Passivation process for superfine aluminum powders obtained by electrical explosion of wires. *Appl. Surf. Sci.* **2003**, *211*, 57-67.

(24) Chung, S. W.; Guliants, E. A.; Bunker, C. E.; Jelliss, P. A.; Buckner, S. W. Size-Dependent Nanoparticle Reaction Enthalpy: Oxidation of Aluminum Nanoparticles. *J. Phys. Chem. Solids* **2011**, *72*, 719-724.

(25) Noor, F.; Zhang, H.; Korakianitis, T.; Wen, D. Oxidation and ignition of aluminum nanomaterials. *Phys. Chem. Chem. Phys.* **2013**, *15*, 20176-20188.

(26) Yoon, T. H.; Johnson, S. B.; Benzerara, K.; Doyle, C. S.; Tyliszczak, T.; Shuh, D. K.; Brown, G. E. In situ characterization of aluminum-containing mineral-microorganism aqueous suspensions using scanning transmission X-ray microscopy. *Langmuir* **2004**, *20*, 10361-10366.

(27) van der Bij, H. E.; Cicmil, D.; Wang, J.; Meirer, F.; de Groot, F. M. F.; Weckhuysen, B. M. Aluminum-Phosphate Binder Formation in Zeolites as Probed with X-ray Absorption Microscopy. *J. Am. Chem. Soc.* **2014**, *136*, 17774-17787.

(28) de Groot, F. M. F.; de Smit, E.; van Schooneveld, M. M.; Aramburo, L. R.; Weckhuysen, B. M. In-situ Scanning Transmission X-Ray Microscopy of Catalytic Solids and Related Nanomaterials. *Chemphyschem* **2010**, *11*, 951-962.

(29) Minasian, S. G.; Keith, J. M.; Batista, E. R.; Boland, K. S.; Bradley, J. A.; Daly, S. R.; Sokaras, D.; Kozimor, S. A.; Lukens, W. W.; Martin, R. L.; Nordlund, D.; Seidler, G. T.; Shuh, D. K.; Tyliszczak, T.; Wagner, G. L.; Weng, T. C.; Yang, P. Covalency in Metal-Oxygen Multiple Bonds Evaluated Using Oxygen K-edge Spectroscopy and Electronic Structure Theory. *J. Am. Chem. Soc.* **2013**, *135*, 1864-1871.

(30) Wen, X.-D.; Loeble, M. W.; Batista, E. R.; Bauer, E.; Boland, K. S.; Burrell, A. K.; Conradson, S. D.; Daly, S. R.; Kozimor, S. A.; Minasian, S. G.; Martin, R. L.; McCleskey, T. M.; Scott, B. L.; Shuh, D. K.; Tyliszczak, T. Electronic structure and O K-edge XAS spectroscopy of U_3O_8. *J. Electron. Spectrosc. Relat. Phenom.* **2014**, *194*, 81-87.

(31) Altman, A. B.; Pemmaraju, C. D.; Camp, C.; Arnold, J.; Minasian, S. G.; Prendergast, D.; Shuh, D. K.; Tyliszczak, T. Theory and X-ray Absorption Spectroscopy for Aluminum Coordination Complexes – Al K-Edge Studies of Charge and Bonding in (BDI)Al, (BDI)AlR_2, and (BDI)AlX_2 Complexes. *J. Am. Chem. Soc.* **2015**, *137*, 10304-10316.

(32) Altman, A. B.; Pacold, J. I.; Wang, J.; Lukens, W. W.; Minasian, S. G. Evidence for 5d-σ and 5d-π Covalency in Lanthanide Sesquioxides from Oxygen K-Edge X-Ray Absorption Spectroscopy. *Dalton Trans.* **2016**, *45*, 9948-9961.

(33) Shadle, S. E.; Hedman, B.; Hodgson, K. O.; Solomon, E. I. Ligand K-edge X-ray absorption spectroscopy as a probe of ligand-metal bonding - charge donation and covalency in copper-chloride systems. *Inorg. Chem.* **1994**, *33*, 4235-4244.

(34) Shadle, S. E.; Hedman, B.; Hodgson, K. O.; Solomon, E. I. Ligand K-Edge X-ray Absorption Spectroscopic Studies: Metal–Ligand Covalency in a Series of Transition-Metal Tetrachlorides. *J. Am. Chem. Soc.* **1995**, *117*, 2259-2272.

(35) Glaser, T.; Hedman, B.; Hodgson, K. O.; Solomon, E. I. Ligand K-edge X-ray absorption spectroscopy: A direct probe of ligand-metal covalency. *Acc. Chem. Res.* **2000**, *33*, 859-868.

(36) George, S. D.; Brant, P.; Solomon, E. I. Metal and Ligand K-Edge XAS of Organotitanium Complexes: Metal 4p and 3d contributions to pre-edge intensity and their contributions to bonding. *J. Am. Chem. Soc.* **2005**, *127*, 667-674.

(37) Solomon, E. I.; Hedman, B.; Hodgson, K. O.; Dey, A.; Szilagyi, R. K. Ligand K-edge X-ray absorption spectroscopy: covalency of ligand-metal bonds. *Coord. Chem. Rev.* **2005**, *249*, 97-129.

(38) Arhammar, C.; Pietzsch, A.; Bock, N.; Holmstroem, E.; Araujo, C. M.; Grasjo, J.; Zhao, S.; Green, S.; Peery, T.; Hennies, F.; Amerioun, S.; Foehlisch, A.; Schlappa, J.; Schmitt, T.; Strocov, V. N.; Niklasson, G. A.; Wallace, D. C.; Rubensson, J.-E.; Johansson, B.; Ahuja, R. Unveiling the Complex Electronic Structure of Amorphous Metal Oxides. *PNAS* **2011**, *108*, 6355-6360.

(39) Mench, M. M.; Kuo, K. K.; Yeh, C. L.; Lu, Y. C. Comparison of thermal behavior of regular and ultra-fine aluminum powders (Alex) made from plasma explosion process. *Combust. Sci. Technol.* **1998**, *135*, 269-292.

(40) Fernando, K. A. S.; Smith, M. J.; Harruff, B. A.; Lewis, W. K.; Guliants, E. A.; Bunker, C. E. Sonochemically Assisted Thermal Decomposition of Alane N,N-Dimethylethylamine with Titanium(IV) Isopropoxide in the Presence of Oleic Acid to Yield Air-Stable and Size-Selective Aluminum Core-Shelll Nanoparticles. *J. Phys. Chem. C* **2009**, *113*, 500-503.

(41) Gromov, A. A.; Forter-Barth, U.; Teipel, U. Aluminum nanopowders produced by electrical explosion of wires and passivated by non-inert coatings: Characterisation and reactivity with air and water. *Powder Technol.* **2006**, *164*, 111-115.

(42) Eliezer, S.; Eliaz, N.; Grossman, E.; Fisher, D.; Gouzman, I.; Henis, Z.; Pecker, S.; Horovitz, Y.; Fraenkel, M.; Maman, S.; Lereah, Y. Synthesis of Nanoparticles with Femtosecond Laser Pulses. *Phys. Rev. B* **2004**, *69*, 144119.

(43) Baladi, A.; Mamoory, R. S. Investigation of Different Liquid Media and Ablation Times on Pulsed Laser Ablation Synthesis of Aluminum Nanoparticles. *Appl. Surf. Sci.* **2010**, *256*, 7559-7564.

(44) Foley, T. J.; Johnson, C. E.; Higa, K. T. Inhibition of Oxide Formation on Aluminum Nanoparticles by Transition Metal Coating. *Chem. Mater.* **2005**, *17*, 4086-4091.

(45) Lewis, W. K.; Rosenberger, A. T.; Gord, J. R.; Crouse, C. A.; Harruff, B. A.; Fernando, K. A. S.; Smith, M. J.; Phelps, D. K.; Spowart, J. E.; Guliants, E. A.; Bunker, C. E. Multispectroscopic (FTIR, XPS, and TOFMS-TPD) Investigation of the Core-Shell Bonding in Sonochemically Prepared Aluminum Nanoparticles Capped with Oleic Acid. *J. Phys. Chem. C* **2010**, *114*, 6377-6380.

(46) Roy, S.; Jiang, N.; Stauffer, H. U.; Schmidt, J. B.; Kulatilaka, W. D.; Meyer, T. R.; Bunker, C. E.; Gord, J. R. Spatially and temporally resolved temperature and shock-speed measurements behind a laser-induced blast wave of energetic nanoparticles. *J. Appl. Phys.* **2013**, *113*, 184310.

(47) Lewis, W. K.; Rumchik, C. G.; Smith, M. J.; Fernando, K. A. S.; Crouse, C. A.; Spowart, J. E.; Guliants, E. A.; Bunker, C. E. Comparison of post-detonation combustion in explosives incorporating aluminum nanoparticles: Influence of the passivation layer. *J. Appl. Phys.* **2013**, *113*, 044907.

(48) Lyashko, A. P.; Ilin, A. P.; Savelev, G. G. Modification of the Surface of Submicron Aluminum Powders. *Russ. J. Appl. Chem.* **1993**, *66*, 999-1001.

(49) Jouet, R. J.; Warren, A. D.; Rosenberg, D. M.; Bellitto, V. J.; Park, K.; Zachariah, M. R. Surface passivation of bare aluminum nanoparticles using perfluoroalkyl carboxylic acids. *Chem. Mater.* **2005**, *17*, 2987-2996.

(50) Chung, S. W.; Guliants, E. A.; Bunker, C. E.; Hammerstroem, D. W.; Deng, Y.; Burgers, M. A.; Jelliss, P. A.; Buckner, S. W. Capping and Passivation of Aluminum Nanoparticles Using Alkyl-Substituted Epoxides. *Langmuir* **2009**, *25*, 8883-8887.

(51) Li, H.; Meziani, M. J.; Lu, F.; Bunker, C. E.; Guliants, E. A.; Sun, Y.-P. Templated Synthesis of Aluminum Nanoparticles - A New Route to Stable Energetic Materials. *J. Phys. Chem. C* **2009**, *113*, 20539-20542.

(52) Meziani, M. J.; Bunker, C. E.; Lu, F.; Li, H.; Wang, W.; Guliants, E. A.; Quinn, R. A.; Sun, Y.-P. Formation and Properties of Stabilized Aluminum Nanoparticles. *ACS Appl. Mater. Interfaces* **2009**, *1*, 703-709.

(53) Li, H.; Meziani, M. J.; Kitaygorodskiy, A.; Lu, F.; Bunker, C. E.; Fernando, K. A. S.; Guliants, E. A.; Sun, Y.-P. Preparation and Characterization of Alane Complexes for Energy Applications. *J. Phys. Chem. C* **2010**, *114*, 3318-3322.

(54) Hammerstroem, D. W.; Burgers, M. A.; Chung, S. W.; Guliants, E. A.; Bunker, C. E.; Wentz, K. M.; Hayes, S. E.; Buckner, S. W.; Jelliss, P. A. Aluminum Nanoparticles Capped by Polymerization of Alkyl-Substituted Epoxides: Ratio-Dependent Stability and Particle Size. *Inorg. Chem.* **2011**, *50*, 5054-5059.

(55) Atmane, Y. A.; Sicard, L.; Lamouri, A.; Pinson, J.; Sicard, M.; Masson, C.; Nowak, S.; Decorse, P.; Piquemal, J.-Y.; Galtayries, A.; Mangeney, C. Functionalization of Aluminum Nanoparticles Using a Combination of Aryl Diazonium Salt Chemistry and Iniferter Method. *J. Phys. Chem. C* **2013**, *117*, 26000-26006.

(56) Miller, H. A.; Kusel, B. S.; Danielson, S. T.; Neat, J. W.; Avjian, E. K.; Pierson, S. N.; Budy, S. M.; Ball, D. W.; Iacono, S. T.; Kettwich, S. C. Metastable nanostructured metallized fluoropolymer composites for energetics. *J. Mater. Chem. A* **2013**, *1*, 7050-7058.

(57) Thomas, B. J.; Bunker, C. E.; Guliants, E. A.; Hayes, S. E.; Kheyfets, A.; Wentz, K. M.; Buckner, S. W.; Jelliss, P. A. Synthesis of aluminum nanoparticles capped with copolymerizable epoxides. *J. Nanopart. Res.* **2013**, *15*, 1729.

(58) Yagodnikov, D. A.; Voronetskii, A. V. Experimental and theoretical study of the ignition and combustion of an aerosol of encapsulated aluminum particles. *Combust. Explos. Shock Waves* **1997**, *33*, 49-55.

(59) Shafirovich, E.; Mukasyan, A.; Thiers, L.; Varma, A.; Legrand, B.; Chauveau, C.; Gokalp, I. Ignition and combustion of Al particles clad by Ni. *Combust. Sci. Technol.* **2002**, *174*, 125-140.

(60) Kwon, Y.-S.; Gromov, A. A.; Strokova, J. I. Passivation of the surface of aluminum nanopowders by protective coatings of the different chemical origin. *Appl. Surf. Sci.* **2007**, *253*, 5558-5564.

(61) Kilcoyne, A. L. D.; Tyliszczak, T.; Steele, W. F.; Fakra, S.; Hitchcock, P.; Franck, K.; Anderson, E.; Harteneck, B.; Rightor, E. G.; Mitchell, G. E.; Hitchcock, A. P.; Yang, L.; Warwick, T.; Ade, H.

Interferometer-controlled scanning transmission X-ray microscopes at the Advanced Light Source. *J. Synchrotron Rad.* **2003**, *10*, 125-136.

(62) Tyliszczak, T.; Warwick, T.; Kilcoyne, A. L. D.; Fakra, S.; Shuh, D. K.; Yoon, T. H.; Brown, G. E.; Andrews, S.; Chembrolu, V.; Strachan, J.; Acremann, Y. In *Synchrotron Radiation Instrumentation 2003, AIP Conference Proceedings* 2004; Vol. 705, p 1356-1359.

(63) Bluhm, H.; Andersson, K.; Araki, T.; Benzerara, K.; Brown, G. E.; Dynes, J. J.; Ghosal, S.; Gilles, M. K.; Hansen, H. C.; Hemminger, J. C.; Hitchcock, A. P.; Ketteler, G.; Kilcoyne, A. L. D.; Kneedler, E.; Lawrence, J. R.; Leppard, G. G.; Majzlan, J.; Mun, B. S.; Myneni, S. C. B.; Nilsson, A.; Ogasawara, H.; Ogletree, D. F.; Pecher, K.; Salmeron, M.; Shuh, D. K.; Tonner, B.; Tyliszczak, T.; Warwick, T.; Yoon, T. H. Soft X-Ray Microscopy and Spectroscopy at the Molecular Environmental Science Beamline at the Advanced Light Source. *J. Electron. Spectrosc. Relat. Phenom.* **2006**, *150*, 86-104.

(64) Haber, J. A.; Buhro, W. E. Kinetic instability of nanocrystalline aluminum prepared by chemical synthesis; Facile room-temperature grain growth. *J. Am. Chem. Soc.* **1998**, *120*, 10847-10855.

(65) Koprinarov, I. N.; Hitchcock, A. P.; McCrory, C. T.; Childs, R. F. Quantitative mapping of structured polymeric systems using singular value decomposition analysis of soft X-ray images. *J. Phys. Chem. B* **2002**, *106*, 5358-5364.

(66) Koski, K.; Holsa, J.; Juliet, P. Properties of aluminium oxide thin films deposited by reactive magnetron sputtering. *Thin Solid Films* **1999**, *339*, 240-248.

(67) Powell, F. R.; Vedder, P. W.; Lindblom, J. F.; Powell, S. F. Thin-Fim Filter Performance for Extreme Ultraviolet and X-Ray Applications. *Opt. Eng.* **1990**, *29*, 614-624.

(68) Fedotova, T. D.; Glotov, O. G.; Zarko, V. E. Chemical analysis of aluminum as a propellant ingredient and determination of aluminum and aluminum nitride in condensed combustion products. *Propell. Explos. Pyrot.* **2000**, *25*, 325-332.

(69) Jelliss, P. A.; Buckner, S. W.; Chung, S. W.; Patel, A.; Guliants, E. A.; Bunker, C. E. The use of 1,2-epoxyhexane as a passivating agent for core-shell aluminum nanoparticles with very high active aluminum content. *Solid State Sci.* **2013**, *23*, 8-12.

(70) Balde, C. P.; Mijovilovich, A. E.; Koningsberger, D. C.; van der Eerden, A. M. J.; Smith, A. D.; de Jong, K. P.; Bitter, J. H. XAFS study of the Al K-edge in $NaAlH_4$. *J. Phys. Chem. C* **2007**, *111*, 11721-11725.

(71) Leon, A.; Balerna, A.; Cinque, G.; Frommen, C.; Fichtner, M. Al K-edge XANES measurements in $NaAlH_4$ doped with $TiCl_3$ by ball milling. *J. Phys. Chem. C* **2007**, *111*, 3795-3798.

(72) Rehr, J. J.; Kas, J. J.; Prange, M. P.; Sorini, A. P.; Takimoto, Y.; Vila, F. Ab initio theory and calculations of X-ray spectra. *C R Phys.* **2009**, *10*, 548-559.

(73) Rehr, J. J.; Kas, J. J.; Vila, F. D.; Prange, M. P.; Jorissen, K. Parameter-free calculations of X-ray spectra with FEFF9. *Phys. Chem. Chem. Phys.* **2010**, *12*, 5503-5513.

(74) Yamamoto, T.; Kudo, T.; Yamamoto, T.; Kawai, J. Analysis of coordination environment of aluminum species in zeolites and amorphous silica-alumina by X-ray absorption and emission spectroscopy. *Microporous Mesoporous Mater.* **2013**, *182*, 239-243.

(75) Benuzzi-Mounaix, A.; Dorchies, F.; Recoules, V.; Festa, F.; Peyrusse, O.; Levy, A.; Ravasio, A.; Hall, T.; Koenig, M.; Amadou, N.; Brambrink, E.; Mazevet, S. Electronic Structure Investigation of Highly Compressed Aluminum with K-Edge Absorption Spectroscopy. *Phys. Rev. Lett.* **2011**, *107*, 165006.

(76) Peyrusse, O. Real-space finite-difference calculations of XANES spectra along the aluminum Hugoniot from molecular dynamics simulations. *High Energ. Dens. Phys.* **2010**, *6*, 357-364.

(77) Nakanishi, K.; Ohta, T. Verification of the FEFF simulations to K-edge XANES spectra of the third row elements. *J. Phys. Condens. Matter* **2009**, *21*, 104214.

(78) Mazevet, S.; Zerah, G. Ab Initio Simulations of the K-Edge Shift along the Aluminum Hugoniot. *Phys. Rev. Lett.* **2008**, *101*, 155001.

(79) Dorchies, F.; Harmand, M.; Descamps, D.; Fourment, C.; Hulin, S.; Petit, S.; Peyrusse, O.; Santos, J. J. High-Power 1 kHz Laser-Plasma X-Ray Source for Ultrafast X-Ray Absorption Near-Edge Spectroscopy in the keV Range. *Appl. Phys. Lett.* **2008**, *93*, 121113.

(80) Wong, J.; George, G. N.; Pickering, I. J.; Rek, Z. U.; Rowen, M.; Tanaka, T.; Via, G. H.; Devries, B.; Vaughan, D. E. W.; Brown, G. E. New Opportunities in XAFS Investigation in the 1-2 keV Region. *Solid State Commun.* **1994**, *92*, 559-562.

(81) Fontaine, A.; Lagarde, P.; Raoux, D.; Esteva, J. M. Soft X-Ray Absorption and EXAFS on the K-Edge of Aluminum. *J. Phys. F: Metal Phys.* **1979**, *9*, 2143-2153.

(82) Albright, T. A.; Burdett, J. K.; Whangbo, M. *Orbital Interactions in Chemistry*; John Wiley and Sons: New York, 1985.

(83) Hoffmann, R. *Solids and Surfaces: A Chemist's View of Bonding in Extended Structures*; Wiley-VCH: New York, 1988.

(84) DeKock, R. L.; Gray, H. B. *Chemical Structure and Bonding*; University Science Books: Sausalito, 1989.

(85) Melko, J. J.; Castleman, A. W., Jr. Photoelectron imaging of small aluminum clusters: quantifying s-p hybridization. *Phys. Chem. Chem. Phys.* **2013**, *15*, 3173-3178.

(86) Stöhr, J. *NEXAFS Spectroscopy*; Springer-Verlag: New York, 2003.

(87) Aramburo, L. R.; Liu, Y.; Tyliszczak, T.; de Groot, F. M. F.; Andrews, J. C.; Weckhuysen, B. M. 3D Nanoscale Chemical Imaging of the Distribution of Aluminum Coordination Environments in Zeolites with Soft X-Ray Microscopy. *Chemphyschem* **2013**, *14*, 496-499.

(88) Ildefonse, P.; Cabaret, D.; Sainctavit, P.; Calas, G.; Flank, A. M.; Lagarde, P. Aluminium X-ray absorption near edge structure in model compounds and Earth's surface minerals. *Phys. Chem. Miner.* **1998**, *25*, 112-121.

(89) Cabaret, D.; Sainctavit, P.; Ildefonse, P.; Flank, A. M. Full Multiple-Scattering Calculations on Silicates and Oxides at the Al K Edge. *J. Phys. Condens. Matter* **1996**, *8*, 3691-3704.

(90) Li, D. E.; Bancroft, G. M.; Fleet, M. E.; Feng, X. H.; Pan, Y. M. Al K-Edge XANES Spectra of Aluminosilicate Minerals. *Am. Mineral.* **1995**, *80*, 432-440.

(91) McKeown, D. A. Aluminum X-Ray Absorption Near-Edge Spectra of Some Oxide Minerals: Calculation Versus Experimental Data. *Phys. Chem. Miner.* **1989**, *16*, 678-683.

(92) Figgis, B. N.; Hitchman, M. A. *Ligand Field Theory and Its Applications*; Wiley-VCH: New York, 2000.

(93) Minasian, S. G.; Keith, J. M.; Batista, E. R.; Boland, K. S.; Kozimor, S. A.; Martin, R. L.; Shuh, D. K.; Tyliszczak, T.; Vernon, L. J. Carbon K-Edge X-ray Absorption Spectroscopy and Time-Dependent Density Functional Theory Examination of Metal-Carbon Bonding in Metallocene Dichlorides. *J. Am. Chem. Soc.* **2013**, *135*, 14731-14740.

(94) Prendergast, D.; Galli, G. X-Ray Absorption Spectra of Water from First Principles Calculations. *Phys. Rev. Lett.* **2006**, *96*, 215502.

(95) England, A. H.; Duffin, A. M.; Schwartz, C. P.; Uejio, J. S.; Prendergast, D.; Saykally, R. J. On the Hydration and Hydrolysis of Carbon Dioxide. *Chem. Phys. Lett.* **2011**, *514*, 187-195.

(96) Pemmaraju, C. D.; Copping, R.; Wang, S.; Janousch, M.; Teat, S. J.; Tyliszcak, T.; Canning, A.; Shuh, D. K.; Prendergast, D. Bonding and Charge Transfer in Nitrogen-Donor Uranyl Complexes: Insights from NEXAFS Spectra. *Inorg. Chem.* **2014**, *53*, 11415-11425.

(97) Giannozzi, P.; Baroni, S.; Bonini, N.; Calandra, M.; Car, R.; Cavazzoni, C.; Ceresoli, D.; Chiarotti, G. L.; Cococcioni, M.; Dabo, I.; Dal Corso, A.; de Gironcoli, S.; Fabris, S.; Fratesi, G.; Gebauer, R.; Gerstmann, U.; Gougoussis, C.; Kokalj, A.; Lazzeri, M.; Martin-Samos, L.; Marzari, N.; Mauri, F.; Mazzarello, R.; Paolini, S.; Pasquarello, A.; Paulatto, L.; Sbraccia, C.; Scandolo, S.; Sclauzero, G.; Seitsonen, A. P.; Smogunov, A.; Umari, P.; Wentzcovitch, R. M. QUANTUM ESPRESSO: a modular and open-source software project for quantum simulations of materials. *J. Phys. Condens. Matter* **2009**, *21*, 395502.

(98) Vanderbilt, D. Soft self-consistent pseudopotentials in a generalized eigenvalue formalism. *Phys. Rev. B* **1990**, *41*, 7892-7895.

(99) Prendergast, D.; Louie, S. G. Bloch-state-based interpolation: An efficient generalization of the Shirley approach to interpolating electronic structure. *Phys. Rev. B* **2009**, *80*, 235126.

(100) Momma, K.; Izumi, F. VESTA 3 for three-dimensional visualization of crystal, volumetric and morphology data. *J. Appl. Crystallogr.* **2011**, *44*, 1272-1276.

For Table of Contents Only

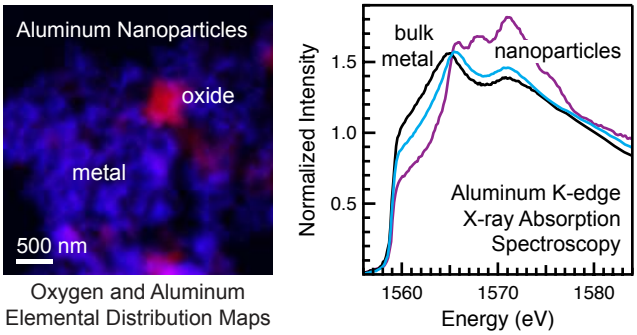

Synopsis: Composition, structure, and thickness of the Al_2O_3 layers on aluminum metal surfaces were determined using X-ray absorption spectroscopy and imaging from a scanning transmission X-ray microscope. The results showed that synthetic strategies including organic passivation may not eliminate surface oxidation, but can be used to tune the chemistry of the oxide layer and control its reactivity. The unique technical approach provided chemical insights that could not be obtained using conventional methods of characterization.